ADVANCED OPTICAL MATERIALS
www.advopticalmat.de

Fe^{3+} Assisted Synthesis of Stable 3D-in-2D $CsPbBr_3/CsPb_2Br_5$ Nanocomposites for Optical Gain Media

Sumit S. Bhosale, Sudhakar Narra, Ruiqi Yang, Aycan Yurtsever, François Légaré, Eric Wei-Guang Diau, and Dongling Ma**

Metal halide perovskite nanocrystals are sought after for many optical and optoelectronic applications, such as light-emitting diode and solar cells, due to their outstanding optical properties. However, their ionic nature makes them susceptible to ambient conditions. One rational solution to this challenge is the passivation or encapsulation of perovskite nanocrystals to isolate them from their environments. Thus, there is an urgent need to develop efficient methods for encapsulating emissive perovskite nanocrystals. A facile post-synthesis method is proposed to treat $Cs_xFA_{(1-x)}PbBr_3$ nanocrystals, in the presence of Fe^{3+} cations, to create a robust and water-stable nanocomposite structure, where 3D $CsPbBr_3$ nanocrystals are embedded in and thus protected by the 2D $CsPb_2Br_5$ nanosheets (named as $CsPbBr_3/CsPb_2Br_5$ hereafter). These Fe^{3+} cations facilitate the formation of the $CsPbBr_3/CsPb_2Br_5$ composite and regulate the growth of 2D $CsPb_2Br_5$ sheets. By performing controlled experiments, the possible mechanism of 2D nanosheet growth is proposed and discussed in detail. More importantly, the composite can remain stable in water for three months and exhibits amplified spontaneous emission under femtosecond laser irradiation. This work presents a synthesis pathway for producing durable perovskite composites that are promising for future lasing applications.

1. Introduction

Lead halide perovskite nanocrystals (PNCs) are omnipresent in scientific research due to their attractive optical and optoelectronic properties.[1] They are rapidly developed and utilized in photovoltaics,[2] light emitting diodes,[3] field-effect transistors,[4] lasing,[5] memory,[6] and photocatalysis applications.[7] PNCs exhibit enhanced photoluminescence (PL), a high absorption coefficient, a tunable band gap, and even more attractively, are defect-tolerant.[8] Additionally, they are easy to synthesize. Schmidt et al. reported the first PNC synthesis method,[9] and since then, ample synthesis methods have been reported. Hot injection[10] and ligand-assisted reprecipitation methods[11] are mostly explored due to their simplicity and ability to produce high-quality PNCs.

3D $APbX_3$ PNCs (A: organic and/or inorganic cations) are divided into organic-inorganic and all-inorganic types, such as methylammonium or formamidinium lead halide ($MAPbX_3$ or $FAPbX_3$) and cesium lead halide ($CsPbX_3$), respectively. These 3D perovskite structures feature corner-sharing $[PbX_6]^{4-}$ octahedra, with the voids formed by four neighboring $[PbX_6]^{4-}$ octahedra being filled by A^+ cations, resulting in cubic or pseudo-cubic structures (**Figure 1**).[8] $MAPbX_3$ PNCs are more prone to degradation due to the low energy of formation, which eventually breaks down into volatile byproducts (CH_3NH_2).[12] In addition, FA-based perovskites are thermally unstable.[13] On the other hand, $CsPbX_3$ PNCs are thermally stable, but the iodine-based ones can undergo phase changes in ambient environments.[13] In our previous work, we reported the synthesis of Cesium-Formamidinium (FA) mixed-cation PNCs ($Cs_xFA_{(1-x)}PbBr_3$) using the hot addition method.[7] These PNCs exhibit fewer surface defects and greater stability due to a halide-rich surface and tuning of tolerance, as well as octahedral factors.[14] However, the stability of all kinds of PNCs in water and humid environments remains a challenging problem to reap the full potential of these materials.

One of the prominent methods for enhancing the chemical stability of emissive PNCs in water is encapsulating them with another robust material.[15] To this end, various organic,[16] inorganic,[17,18] and perovskite[19] based shells have been

S. S. Bhosale, R. Yang, A. Yurtsever, F. Légaré, D. Ma
Center Énergie Matériauxet Télécommunications
Institut National de la Recherche Scientifique (INRS)
Varennes, QC J3X 1P7, Canada
E-mail: dongling.ma@inrs.ca
S. Narra, E. W.-G. Diau
Department of Applied Chemistry and Institute of Molecular Science
National Yang Ming Chiao Tung University
1001 Ta-Hsueh Rd., Hsinchu 30010, Taiwan
E-mail: diau@nycu.edu.tw
S. Narra, E. W.-G. Diau
Center for Emergent Functional Matter Science
National Yang Ming Chiao Tung University
1001 Ta-Hsueh Rd., Hsinchu 30010, Taiwan

The ORCID identification number(s) for the author(s) of this article can be found under https://doi.org/10.1002/adom.202401470

DOI: 10.1002/adom.202401470

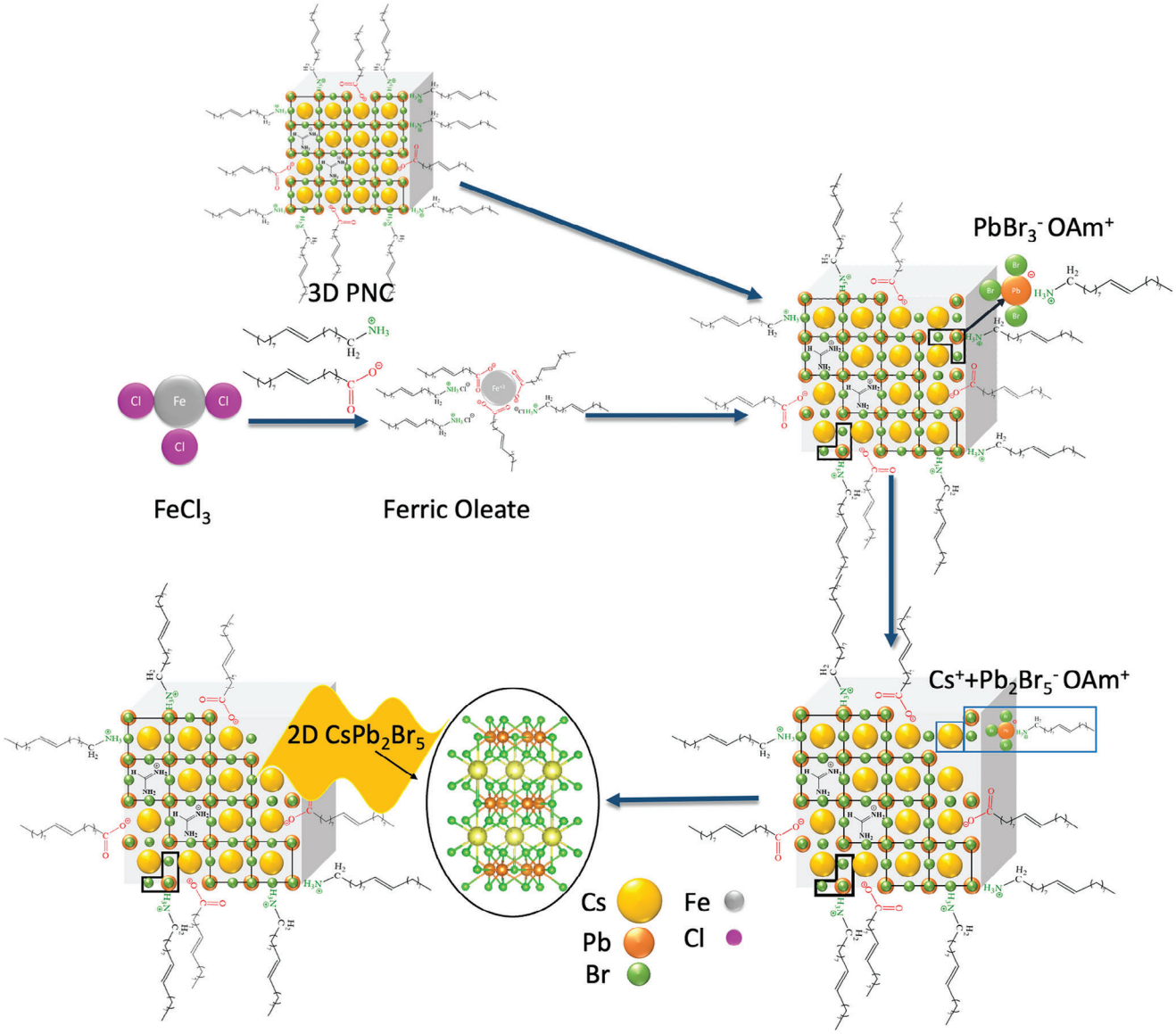

Figure 1. Schematic representation of post-synthetic encapsulation of $CsPbBr_3$ PNC by the 2D $CsPb_2Br_5$ through in situ structural transformation assisted by Fe^{3+} ions.

investigated. However, achieving robust encapsulation of PNCs without introducing excessive defects poses a significant challenge, necessitating a minimal lattice mismatch. Otherwise, water stability may be compromised, and the desired optical properties of PNCs could also be significantly affected. In this regard, 2D structured $CsPb_2Br_5$, where Cs^+ ions are sandwiched between the layers of $[Pb_2Br_5]^-$ with a tetragonal crystal structure (Figure 1), appears as the most promising shell material to protect ionic PNCs. The 2D $CsPb_2Br_5$ material, with a wide band gap of 3.23 eV,[20] can form a type I heterojunction with PNCs (bandgap: 3–1.8 eV).[10] In principle, this configuration does not affect the radiative recombination of PNCs, as the charge carriers remain confined within the PNCs. Moreover, the 2D layered $CsPb_2Br_5$ possesses an indirect band gap, making its photoluminescence in the visible range negligible compared to that of the PNCs.[21] The 2D $CsPb_2Br_5$ structure could be directly synthesized from the $CsPbBr_3$ due to a small difference in their formation energy, possibly leading to the "seamless" interface. It was achieved in some previous work by altering the feeding ratio of Cs and Pb where an excess amount of lead bromide was used.[20] Recently, Prieto et al. reported core-shell formation by heating a reaction mixture at 250 °C after cesium oleate injection;[19] while Kamath et al. reported dodecyl dimethylammonium bromide-induced structure transformation.[22] Apart from the examples mentioned above, water-based,[23] thiol-based,[24] and TEOS-based transformations[25] are also being explored. However, none of them exhibit the capability to tune the lateral dimensions of $CsPb_2Br_5$ 2D sheets, which is a crucial aspect for their application in optoelectronics and photocatalysis, where lateral dimensions can play a role in

charge and mass transfer, affect overall contact resistance in film samples, etc.

In our work, we report a post-synthetic method to encapsulate perovskite nanocrystals with 2D $CsPb_2Br_5$ using Fe^{3+}cations as structural transformation inducers. We avoided the addition of excess toxic lead precursors and replaced them with the Fe^{3+}-oleylamine /oleic acid complex, which is cost-effective and less toxic. The use of Fe^{3+} ions not only induces the formation of 2D $CsPb_2Br_5$ in situ surrounding the 3D PNCs but also allows us to change the lateral size of the $CsPb_2Br_5$ sheets by varying the feeding ratio of the Fe^{3+} complex during post-synthesis treatment. The $CsPb_2Br_5$-encapsulated PNCs remained stable in water for over three months, retaining their optical properties such as absorptions and emissions. We studied the optical gain properties of the encapsulated PNCs using PL and transient absorption spectroscopy (TAS). The PNCs encapsulated within the 2D $CsPb_2Br_5$ nanosheets exhibit excellent stability in water, and the nanosheets amplify spontaneous emission sufficiently, even though it was reported previously that 2D encapsulation contributes to electron deficiency in the PNCs.[20]

2. Results and Discussion

PNCs were synthesized using a previously reported hot addition method (see Figure S1, Supporting Information).[7] In current synthesis formamidinium (FA) bromide precursor was replaced with the mixture of FA acetate and hydrobromic acid in 2-propanol. Hydrobromic acid assists in dissolving FA acetate and provides surplus bromide ions, which are necessary to eliminate surface defects and ensure stability during post-synthesis treatment.[18] During the synthesis, the FA concentration was adjusted to a 1:1 ratio with Cs-oleate. In the post-synthesis treatment, $FeCl_3$ was first heated up in the presence of 0.5 mL of oleic acid (OA) and oleylamine (OLA) in 10 mL of 1-octadecene. The solution was then kept at 100 °C under vacuum until the $FeCl_3$ completely dissolved. To this hot Fe^{3+} solution, the crude PNC solution obtained from the hot addition method was added, and the entire mixture was then heated up to 230 °C. Different percentages (25, 50, and 100%) of $FeCl_3$, with respect to the lead used for the initial synthesis of the PNCs, were fed into the reaction. For comparison, the crude PNC solution was also heated up to 230 °C in the presence of OA-OLA but without $FeCl_3$. For simplification, we use CF0, CF25, CF50, and CF100 to denote the final perovskite samples undergoing 0, 25, 50, and 100% $FeCl_3$ treatment, respectively.

Figure 1 illustrates the structural transformation process from the initial PNCs to the final 3D-in-2D product. We hypothesize that forming Fe oleate leads to the production of oleylammonium chloride. At higher temperatures, oleylammonium cations could react with $PbBr_3^-$ ions, which are present in the perovskite structure. The $PbBr_3$-OLA complex then reacts with $PbBr_2$ to form $Pb_2Br_5^-$ ions that subsequently react with Cs to form the 2D structured $CsPb_2Br_5$. We monitored the reaction at different temperatures to provide evidence for the formation of $Pb_2Br_5^-$ ions. In a Fe-oleate and oleylammonium chloride solution, we added crude PNC solution and extracted 1 mL of the reaction mixture at various temperatures. Figure S2a (Supporting Information) displays the absorbance, normalized to the excitonic peak of PNC, of the crude reaction mixture containing PNC, Fe-oleate, and OLA cation. Initially, a shoulder at ≈343 nm was observed, indicating the formation of $Pb_2Br_5^-$ ions. This shoulder signal diminishes as the reaction temperature increases, attributed to the formation of 2D $CsPb_2Br_5$, which is reflected as a peak (383 nm) appearing at 200 °C.[20] To observe the formation of $Pb_2Br_5^-$ ions, we centrifuged the crude reaction mixture to remove PNCs and formed 3D-in-2D sheets. The absorption spectra of the supernatant are presented in Figure S2b (Supporting Information). It shows a distinct shoulder at 345 nm, indicative of $Pb_2Br_5^-$ ions,[22] which diminishes with increasing temperature, as observed in the absorbance of the crude reaction mixture. The formation of ammonium-based $CsPb_2Br_5$ has indeed been reported previously.[22,26] So, in our experiment, 2D structured $CsPb_2Br_5$ was synthesized without the addition of any extra precursors of Pb and Cs, indicating that $CsPb_2Br_5$ was formed from the $Cs_xFA_{(1-x)}PbBr_3$ structure.

TEM images and XRD analysis of the synthesized samples are presented in **Figure 2**. The TEM image of $Cs_xFA_{(1-x)}PbBr_3$ PNCs shows their uniform cubic morphology, consistent with our previous report.[7] A gradual increase in the size of newly formed nanosheets was observed from 0% to 100% Fe^{3+} treatment. Additional TEM images provided in Figures S3a–d (Supporting Information) reveal the increase in the sheets' lateral dimension from ≈200 nm to several µm from CF25 to CF100, with CF50 showing a size of up to 1 µm, whereas the CF0 sample exhibits significant aggregation due to heat treatment.[27] Thin nanosheets of CF100 samples shown in Figure S3d (Supporting Information) exhibit a wavelike pattern due to electron bombardment during TEM analysis.

We further analyzed the size distribution of 3D PNCs, which seem embedded in the 2D sheets (Figure S4, Supporting Information). The average sizes of 3D PNCs were 21 ± 4.9, 19 ± 5.3, 18 ± 3.4, and 24 ± 6.2 nm for CF0, CF25, CF50, and CF100, respectively. Notably, due to the post-synthesis heat treatment, the $CsPbBr_3$ PNCs (i.e., CF0) exhibit a larger average size compared to the pristine $Cs_xFA_{(1-x)}PbBr_3$ (8.2 ± 1.1 nm).[7] The thickness of 2D $CsPb_2Br_5$ nanosheets was analyzed by atomic force microscopy (AFM). The images and height distribution of the nanosheets, presented in Figure S5 (Supporting Information), show that the average thickness of CF25, CF50, and CF100 is 15.2 ± 2.9, 14.7 ± 3.1 and 19.3 ± 6.6 nm, respectively. The elemental composition of the formed complex structure was probed by TEM-EDX measurements (Figure S6, Supporting Information) with the obtained composition listed in Table S1 (Supporting Information). CF0 represents a 1:1:3.3 ratio of Cs:Pb:Br, which is similar to the standard perovskite structure, as expected. Interestingly, $Cs_xFA_{1-x}PbBr_3$ PNCs were converted to $CsPbBr_3$ by the post-synthesis heat treatment at 230 °C. The organic FA cation is volatile, and it starts to degrade ≈200 °C[28] compared to Cs, leading to its loss during the heating process.[13] However, PNC remains stable due to the excess bromide ions in the solution. Nag and co-workers have also reported a similar strategy for stabilizing PNCs during post-synthesis treatment.[18] TEM-EDX results of CF25 show slight chlorine doping in the perovskite structure due to $FeCl_3$ treatment. In subsequent samples, chlorine concentration increases as the percentage of $FeCl_3$ increases. However, a clear structural change was observed in CF100. The elemental composition is 1:1.9:5.7 for Cs:Pb:Br/Cl, indicating a prominent presence of 2D $CsPb_2Br_5$ and the increase in chloride

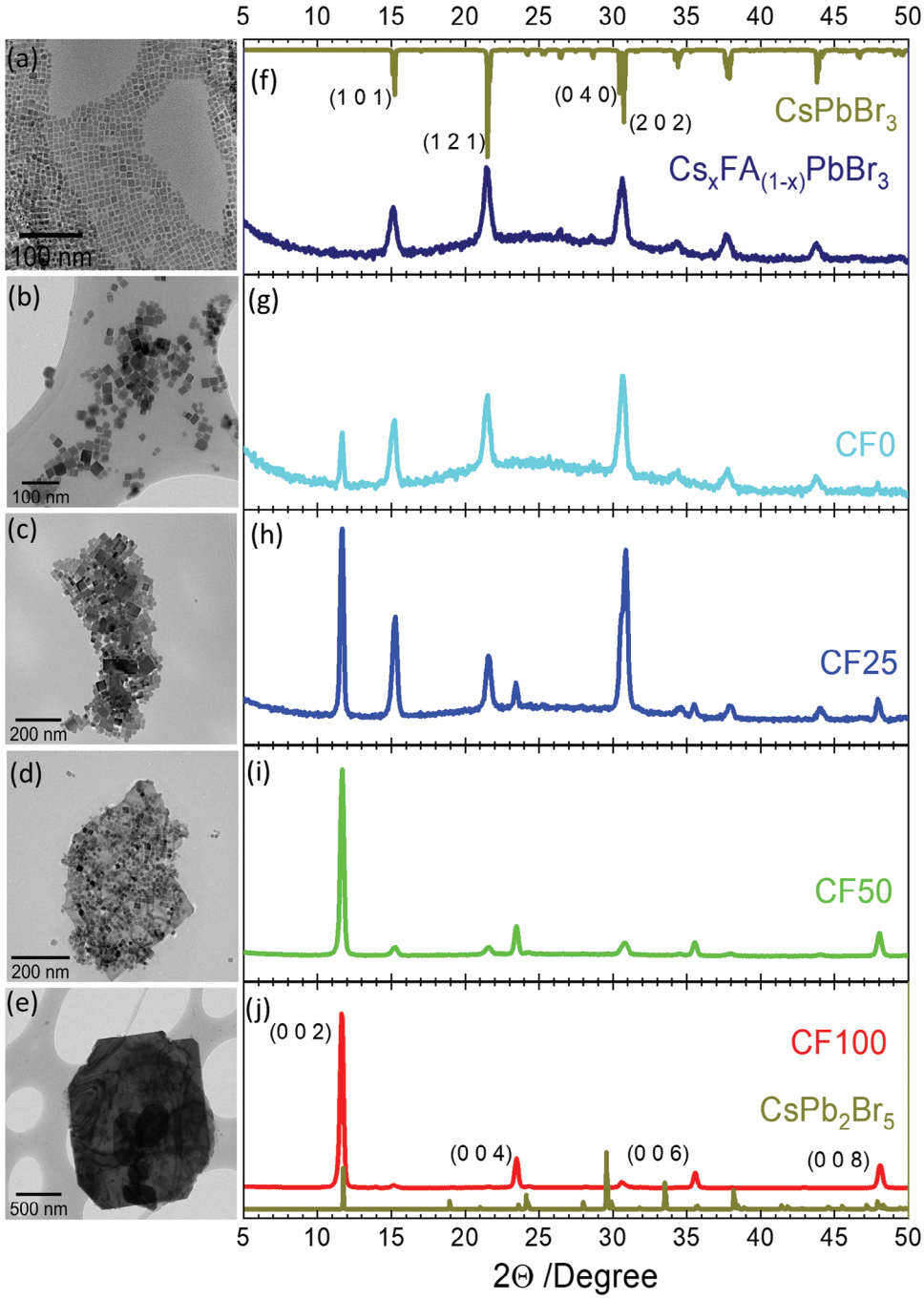

Figure 2. TEM images of a) $Cs_xFA_{(1-x)}PbBr_3$ PNCs before the post-synthesis treatment, b) CF0, c) CF25, d) CF50, and e) CF100; their respective XRD diffraction patterns are shown at the right f–j). Standard XRD patterns of the orthorhombic phase of $CsPbBr_3$ (presented at the top in an inverted form) and the tetragonal phase of $CsPb_2Br_5$ (presented at the bottom) were obtained from the literature.[29,30]

concentration led to the formation of mixed halide perovskite structure. We also detected small quantities of Fe^{3+}, possibly because the tolerance and octahedral factor do not allow many smaller Fe^{+3} ions to integrate into the perovskite structure. Solvated Fe^{3+} species in solution following the heat treatment can be reflected by the color of the solution, where we observed a clear, dark brown solution free of any precipitate. Figure S7a (Supporting Information) shows a photograph of a centrifugation tube containing Fe Oleate- oleylammonium chloride mixture before the post-synthesis treatment (blank), while Figure S7b (Supporting Information) shows the supernatant and the yellow CF50 precipitate after centrifugation. Both the Fe Oleate- oleylammonium chloride mixture and supernatant of CF50 appear similarly dark brown due to the presence of Fe-containing molecules. The negligible change in color between a blank and the supernatant suggests that most of the Fe^{3+} cations neither integrated into the

perovskite crystalline structure nor anchored to its surface. In other words, although Fe^{3+} ions are essential for the dramatic structural transformation, most remained in the solution after the treatment.

The XRD patterns presented in Figure 2 reveal that except for $Cs_xFA_{(1-x)}PbBr_3$ PNCs, all the samples consist of tetragonal $CsPb_2Br_5$ and orthorhombic $CsPbBr_3$ crystalline structures. $Cs_xFA_{(1-x)}PbBr_3$ PNCs are solely orthorhombic with the Pnma space group. CF0, obtained by heating the crude PNC solution at 230 °C in the presence of OA-OLA but without $FeCl_3$, exhibits dominant features of the orthorhombic crystal structure with a clear contribution of the 2D tetragonal structure. The tetragonal structure arises due to excess FA cations reacting with PNCs at the higher temperature (230 °C), following a similar reaction pathway as the OLA cation depicted in Figure 1. To verify this, we conducted a control experiment by heating standard, completely inorganic $CsPbBr_3$ PNCs, which do not contain any FA cations, in the presence of 0.5 mL of OA+OLA at the same temperature (230 °C). The results, presented in Figure S8 (Supporting Information), show that in the absence of FA cations, the tetragonal 2D phase is absent, and instead, the formation of trigonal Cs_4PbBr_6 perovskite was observed, as reported by Alivisatos and co-workers.[31] The peak appearing at 11.6^0, corresponding to the (0 0 2) plane of tetragonal $CsPb_2Br_5$, gradually increases with an increase in the nominal $FeCl_3$ percentage, while the peak appearing at 30.8^0, corresponding to the (0 4 0) plane of orthorhombic $CsPbBr_3$, continues to decrease, suggesting increase in 2D structure's contribution to the diffraction signal of the 2D/3D composite. All the prepared samples show the (0 0 *l*) diffraction peak of the $CsPb_2Br_5$ structure, suggesting that the samples contain the perovskite materials showing a nanosheet morphology.[30,32] To evaluate the significance of Fe^{3+} ions in the formation of the 2D structured $CsPb_2Br_5$ nanosheets, the as-prepared, organic–inorganic hybrid $Cs_xFA_{(1-x)}PbBr_3$ PNCs (ie crude PNCs, before any post-synthesis treatment, in this manuscript) were substituted with completely inorganic $CsPbBr_3$ PNCs for the 50% $FeCl_3$ treatment. Figure S9 (Supporting Information) displays the formation of 2D $CsPb_2Br_5$ instead of triagonal Cs_4PbBr_6. This indicates that $FeCl_3$ can increase the concentration of oleylammonium chloride, which then induces the formation of $Pb_2Br_5^-$ ions, resulting in the final formation of 2D tetragonal $CsPb_2Br_5$, as depicted in Figure 1. Thus, the presence of either FA cation or Fe^{3+} cations is essential for forming the 2D structure, while their co-presence can facilitate the formation of the 2D layered structure. Moreover, by varying the $FeCl_3$ concentration, we can change the average lateral size of the 2D sheets from ≈200 nm to several micrometers.

Figure 3 illustrates the absorption and photoluminescence spectra of the synthesized perovskite samples. As per a previous report by Szafrański and co-workers,[21] these optical spectra are exclusively related to the PNCs in the composite samples because the 2D layered $CsPb_2Br_5$ possesses an indirect band gap, making its photoluminescence in the visible range negligible. The absorption spectra show band edges in the green region with characteristic excitonic peaks observed at 511, 496, 496, and 478 nm for CF0, CF25, CF50, and CF100, respectively. Similarly, the PL spectra displayed emission from the excitonic bands at 518, 500, 502, and 482 nm for CF0, CF25, CF50, and CF100, respectively. The excitonic absorption and emission band positions and bandwidths of CF0 resemble that of $CsPbBr_3$ PNCs published elsewhere.[10] However, a hypsochromic shift was observed in both absorption and PL spectra of other samples with an increase in the percentage of $FeCl_3$ applied during the treatment, highly likely attributed to the increase in chloride doping in the perovskite structure as supported by TEM-EDX data (Figure S6, Table S1, Supporting Information).[33,34] The photoluminescence quantum yield (PLQY) of $Cs_xFA_{(1-x)}PbBr_3$ PNC and composite samples was determined by a relative optical method using coumarin 153 (C153) as the standard.[35] The PLQY of $Cs_xFA_{(1-x)}PbBr_3$ PNC, CF0, CF25, and CF50 was measured as 50%, 35%, 19%, and 18%, respectively (Figure S10, Table S2, Supporting Information). The transient photoluminescence decay profile of the samples, acquired through time-correlated single photon counting (TCSPC), is presented in Figure S11 (Supporting Information). Exponential fitting (Table S3, Supporting Information) reveals that CF0, despite having a lower PLQY than $Cs_xFA_{(1-x)}PbBr_3$ PNC, exhibited a longer PL lifetime (114.7 ns), probably due to shallow trap states involving trapping and de-trapping processes.[36] In contrast, CF25 and CF50 samples showed shorter τ_1 lifetimes (radiative recombination) compared to $Cs_xFA_{(1-x)}PbBr_3$ PNC. The CF50 sample (1.6 ns) exhibited a shorter lifetime compared to CF25 (7.4 ns), indicating that defects due to the post-synthesis treatment are contributing to the decrease in lifetime in these samples.[37] The color of the samples also becomes less yellow from CF0 to CF100 (Figure S12, Supporting Information) due to the increased presence of 2D $CsPb_2Br_5$. However, the scattering in absorption spectra also increases due to the increase in sheet size.

3D-in-2D perovskite composites were then examined for stability in water. Unlike other studies[19] where a toluene solution of PNCs was added to water, we opted for a more direct approach in this work, ie., direct dispersion of the powders in water. We did so because the immiscibility of toluene can protect PNCs, potentially leading to misleading data. The concentration of 3D-in-2D perovskite composite in water, in our case, was adjusted to 1 mg mL^{-1}, and the study was conducted for up to 94 days. The corresponding absorption spectra are presented in Figures 3e–h, while Figures S13a–d (Supporting Information) display the photoluminescence spectra. CF50 remains stable for up to 94 days, whereas all other PNCs considerably degraded over time, with CF100 degrading the fastest. Except for CF100, all other samples could maintain their characteristic excitonic absorption features for up to 43 days, attributed to the 3D PNCs present in these samples. However, after this period, they began to lose this absorption, except for CF50. CF100 degraded the fastest, losing its excitonic absorption after 8 days. Interestingly, CF50 retained its fluorescence from the first day, exhibiting a consistent peak position and peak full-width half maximum (FWHM) between 16 and 17 nm. (Figure S13c, Supporting Information) This stable parameter of CF50 in water makes it a good choice for imaging in aqueous medium.

To better understand how the structure evolves, which leads to the photoluminescence decay in water, TEM images (Figure S14, Supporting Information) were taken for water-dispersed CF50 and CF100 samples, which represent the most and least stable samples, respectively. For the TEM experiment, CF50 and CF100 powders were dispersed in water and subjected to rigorous sonication multiple times to accelerate the degradation process.

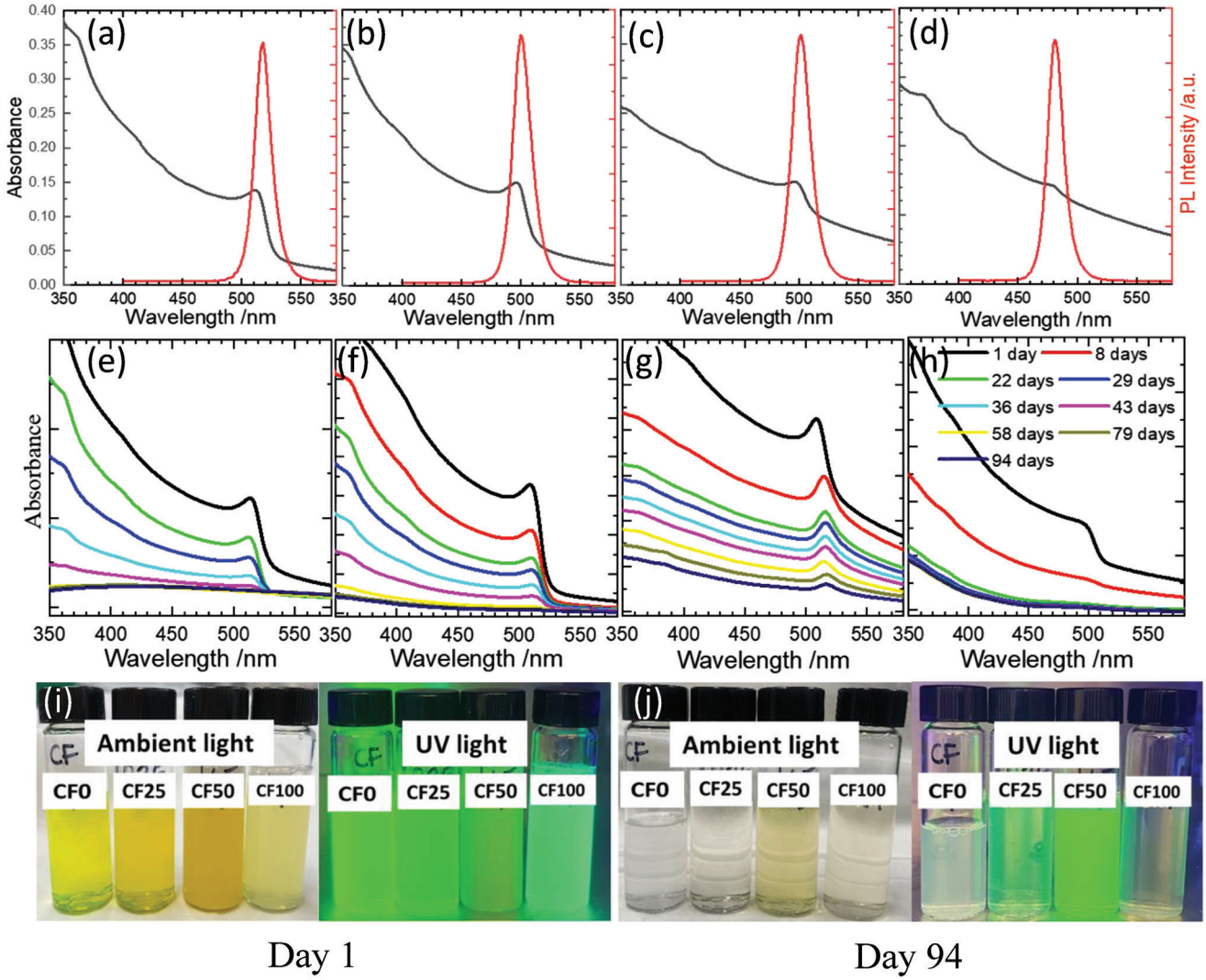

Figure 3. Absorption and photoluminescence spectra of a) CF0, b) CF25, c) CF50, and d) CF100. A stability study was conducted by dispersing PNC powder in water, and absorption spectra were recorded from day 1 to day 94 for e) CF0, f) CF25, g) CF50, and h) CF100. Photograph of composite powder dispersed in water (1 mg mL^{-1}) under typical lab light and UV light on i) Day 1 and j) Day 94. In the latter case, the solution color is due to perovskite emission.

Images in Figure S14a (Supporting Information) reveal the presence of 3D structured $CsPbBr_3$ PNCs inside the nanosheets of the CF50 sample. The retaining of cubic $CsPbBr_3$ confirms that the nanosheets play an essential role in protecting water-labile PNCs by covering them. However, the images of CF100 (Figure S14b, Supporting Information) only show a very small number of cubic $CsPbBr_3$ PNCs in the area of the 2D sheets; instead, many tiny PNCs were scattered in the nanosheet-free area. It is possible because, in CF100, PNCs are situated on the surface of, rather than inside, the 2D $CsPb_2Br_5$, rendering them more susceptible to degradation in the presence of water. To confirm our assumption, we took TEM images by tilting the sample to various angles to probe the position of PNCs with respect to the 2D $CsPb_2Br_5$. Based on our results from Figure S15 (Supporting Information), CF50 at various angles shows that PNCs are covered with a 2D layer, whereas in CF100, the connection between PNCs and 2D sheets is visible with changing angles, confirming that PNCs are attached on the surface of 2D $CsPb_2Br_5$.

The amount of oleylammonium cations produced during the post-synthesis treatment may affect the reaction rate and thereby the encapsulation status of PNCs. If the reaction mixture produces an insufficient number of oleylammonium cations, then $Cs_xFA_{(1-x)}PbBr_3$ PNCs are partially converted to 2D $CsPb_2Br_5$ and encapsulated by the 2D sheet (CF50). However, in the case of a large number of oleylammonium cations generated in a short time, most of the $Cs_xFA_{(1-x)}PbBr_3$ PNCs are rapidly converted to large 2D $CsPb_2Br_5$, and unreacted PNCs occupy the surface of the 2D sheets (CF100).

As the samples showed bright photoluminescence characteristics (Figure 3) and $CsPbBr_3$ PNCs are known for their optical gain characteristics with a broad range of optical gain thresholds, depending on the structure of the PNC,[38–47] the optical gain characteristics of CF0, CF25, CF50, and CF100 samples were

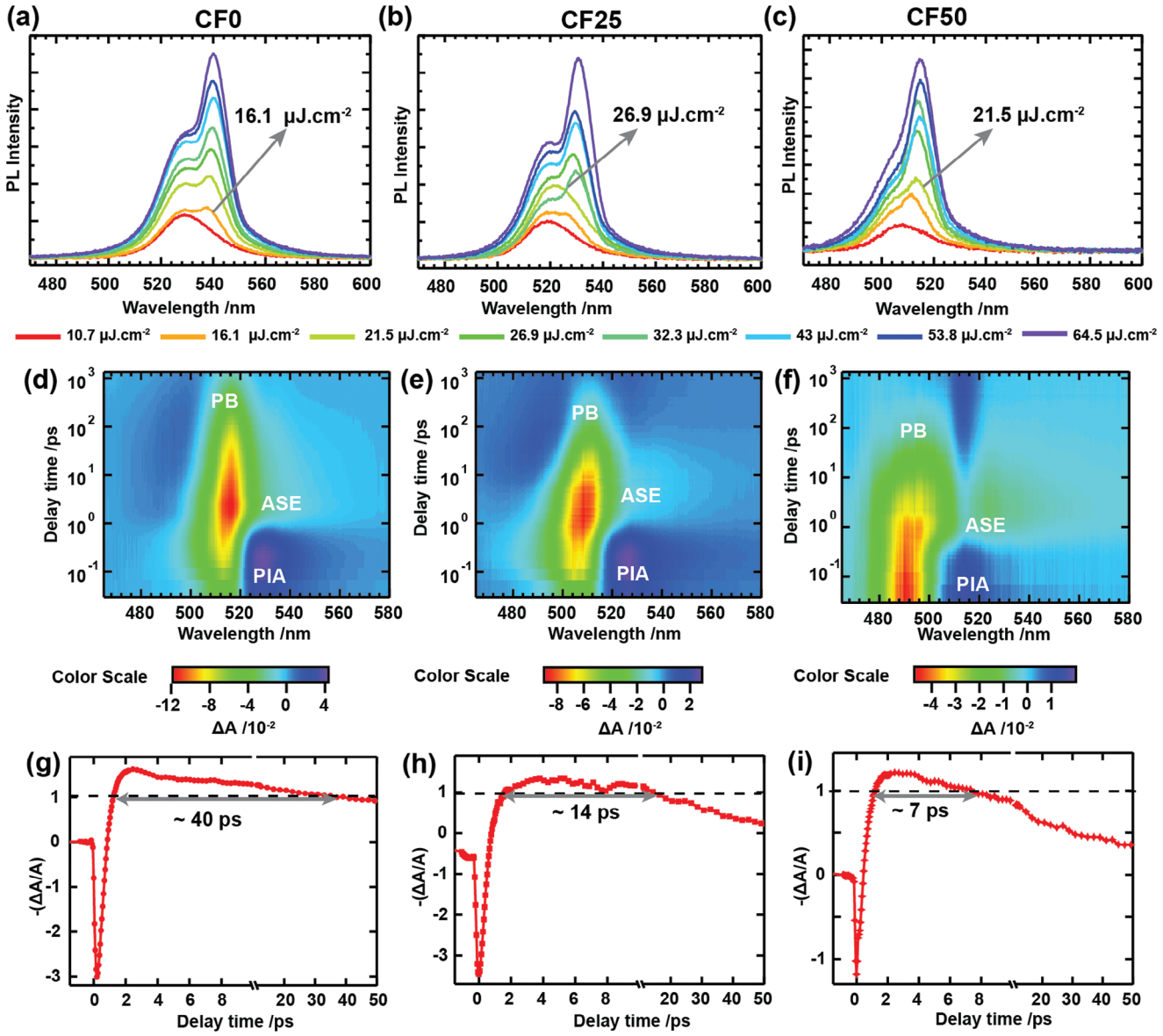

Figure 4. Fluence-dependent photoluminescence spectra of a) CF0, b) CF25, and c) CF50, show the evolution of amplified spontaneous emission bands with an increase of laser fluence. Femtosecond transient absorption spectrograms of d) CF0, e) CF25, and f) CF50 acquired at fluences above the threshold of the amplified spontaneous emission. PB: photobleach, PIA: photoinduced absorption, and ASE: amplified spontaneous emission. ASE lifetimes of g) CF0, h) CF25, and i) CF50 were measured at 536, 530, and 522 nm, respectively.

assessed by measuring the fluence-dependent PL spectra, as shown in **Figures** 4a–c. Optical gain measurements were carried out on thin-film samples prepared by drop-casting a solution of 3D-in-2D perovskite composite in toluene onto 2 × 2 cm glass substrates. The concentration of composites was adjusted to 1 mg mL^{-1}. Films were deposited by slowly evaporating the solvent without heating (Figure S12, Supporting Information). Top-view scanning electron microscopy images of the thin films (Figure S16, Supporting Information) show that the composite forms a compact film, except for CF100 due to the large 2D sheet dimensions. Among all the films, the one formed by CF50 is the most compact and has fewer cracks and pinholes. The fluence-dependent PL spectra of CF0, CF25, and CF50 samples showed a build-up of red-shifted, narrowed emission bands on top of the intrinsic excitonic emission bands observed under lower fluence, with a rapid increase of intensity compared to the native bands. The observed bandwidths of the narrow emission bands (Figure 4a) are ≈10 nm for all three samples, and they display characteristic peak shifts of ≈10–12 nm from the intrinsic emission band. These narrowed emission bands were assigned to amplified stimulated emission (ASE) bands in PNCs.[38–47] The origin of ASE bands in PNCs has been assigned to biexcitonic emissions,[48,49] doping, and trap states.[37,50] The ASE threshold fluences were determined to be 16.1, 26.9, and 21.5 μJ cm^{-2} for CF0, CF25, and CF50 samples, respectively. The ASE thresholds reported here

are within the range of the reported values for $CsPbBr_3$ PNCs (Table S4, Supporting Information). It is worth mentioning that neither pristine $Cs_xFA_{(1-x)}PbBr_3$ nor CF100 produced any ASE bands. We believe it is because of the minimal defects in the case of $Cs_xFA_{(1-x)}PbBr_3$,[7,14] while the formation of 3D-in-2D heterojunction highly likely produces "useful" interfacial defects, which are responsible for the observed ASE in the three samples of CF0, CF25, and CF50.[37] Defects in perovskite materials can trap carriers, thereby stabilizing them in the excited state to achieve population inversion.[37,51] However, the trapping rate must remain lower than the Auger recombination rate to ensure effective optical gain. As for CF100, it mainly had the 2D structure (Figure 2; Figure S3d, Supporting Information) with a dramatic difference in the Cs-to-Pb ratio from all other samples (Table S1, Supporting Information).

Further, femtosecond transient absorption spectroscopic experiments were conducted to probe the optical gain lifetimes as optical gain can only be realized when population inversion is built up faster than the competing recombination pathways such as Auger recombination, band-band recombination, etc.[51] The TAS spectrograms of CF0, CF25, and CF50 are shown in Figures 4d–f. They show a typical photobleach band (PB), photoinduced absorption bands (PIA), and ASE bands. The PB band signals (with peak position varying in the range of 514–496 nm for the three samples) display the recovery of the excitonic states and the PIA bands (centered ≈528, 526, and 513 nm for CF0, CF25, and CF50 respectively) display rapid recovery of the thermalized population of excitons/carriers. The ASE band signals display the recovery of optical gain mixed with that of PIA bands and PB band tail states, and their transient kinetics were examined to gain more insights into the time scales of the optical gain (Figures 4g–i). The normalized transient kinetics of the ASE band monitored at 536 nm for CF0, 530 nm for CF25, and 522 nm for CF50 with absorbance (-ΔA/A) show a rapid spike due to thermalization, followed by a population buildup and then population recombination due to Auger or other competing recombination processes.[51] The population buildup time can be assessed as an optical gain time of the PNCs measured here. The optical gain time constants for CF0, CF25, and CF50 samples are 40, 14, and 7 ps, respectively. These values are comparable to the 35 ps optical gain time reported for $CsPbBr_3$ PNC samples.[52] The higher ASE thresholds and faster optical gains of CF25 and CF50 samples compared to CF0 are likely due to competing optical loss recombination processes induced by interfacial defects created during the $FeCl_3$ treatment. Nevertheless, the CF25 and CF50 samples were brighter and also more stable in water than the CF0 samples (Figure 3). Considering the tradeoff between water stability and ASE thresholds, CF25 and CF50 PNCs are considered attractive candidates for lasing in harsh environmental conditions and highly likely also for other applications, such as bio-imaging.

3. Conclusion

In summary, four different types of perovskite composites were synthesized by simply treating as prepared $Cs_xFA_{(1-x)}PbBr_3$ PNC solution with varying percentages of $FeCl_3$, with respect to the Pb concentration used for $Cs_xFA_{(1-x)}PbBr_3$ synthesis, at the elevated temperature. Such produced samples are named as CF0, CF25, CF50, and CF100, representing 0, 25, 50, and 100% $FeCl_3$ treatment, respectively. All the samples exhibit orthorhombic and tetragonal crystal structures, corresponding to 3D $CsPbBr_3$ and 2D layered $CsPb_2Br_5$, respectively. In contrast, as synthesized $Cs_xFA_{(1-x)}PbBr_3$ PNCs show only orthorhombic crystal structure. The tetragonal phase increases with increasing Fe^{3+} ions in post-synthesis treatment, indicating the increased transformation from 3D $Cs_xFA_{(1-x)}PbBr_3$ PNCs to the 2D $CsPb_2Br_5$ sheets. During the post-synthesis treatment, $FeCl_3$ reacts with OA+OLA to form Fe oleate and oleylammonium chloride. The oleylammonium cation then reacts with the perovskite structure at higher temperatures to form $Pb_2Br_5^-$, inducing the formation of $CsPb_2Br_5$ nanosheets. Due to this in situ structure transformation process, the 3D structured $CsPbBr_3$ PNCs are partially encapsulated, if not completely, by the 2D structured $CsPb_2Br_5$ nanosheets. Thanks to the formation of this 3D-in-2D structure, the optimal sample of CF50 exhibits excellent stability in water, keeping well-defined excitonic absorption and emission for up to 94 days, comparable to what was reported by Prieto et al.[19] This opens the door for PNCs to be used in many applications, including, but not limited to, bioimaging and photocatalysis. We further explored their application in lasing. Except for CF100, all the samples exhibited considerable optical gain. The ASE threshold fluences were determined to be 16.1, 26.9, and 21.5 μJ cm^{-2}, and the optical gain time constants were found to be 40, 14, and 7 ps for CF0, CF25, and CF50, respectively. CF25 and CF50 exhibited slightly higher ASE thresholds and shorter optical gain constants, highly likely due to the presence of trap states at the 3D and 2D interface and the presence of more optically inactive, indirect bandgap 2D $CsPb_2Br_5$ matrix, which do not contribute to ASE. However, the stability provided by the 2D sheets makes CF25 and CF50 robust candidates for laser materials preparation, manipulation, and operation. In summary, the current work provides a simple method for creating water-stable PNCs, which so far is difficult to achieve and thereby enables their many applications in aqueous systems or where stability in air with the presence of moisture is required.

4. Experimental Section

Materials: All commercial materials were used without further purification: lead bromide ($PbBr_2$, 99%, Sigma–Aldrich), cesium carbonate (Cs_2CO_3, 99%, Sigma–Aldrich), formamidine acetate salt ($HN{=}CHNH_2CH_3COOH$, 99%, Sigma–Aldrich), hydrobromic acid (HBr, 48%, Sigma–Aldrich), Iron(III) chloride hexahydrate ($FeCl_3$, 97%, Sigma–Aldrich) oleyl amine (OLA, technical grade, 70%, Sigma–Aldrich), oleic acid (OA, technical grade, 90%, Sigma–Aldrich), toluene (anhydrous, 99.8%, Sigma–Aldrich), 2-propanol (anhydrous, 99.5%, Sigma–Aldrich).

Preparation of Cesium Oleate (Cs oleate) and Formamidinium Solution: Cesium carbonate (Cs_2CO_3, 0.94 mmol), oleic acid (OA, 3 mL), and octadecene (3 mL) were added to a vial (20 mL). This solution was heated at 150 °C until the solution became transparent. To prepare the formamidinium solution, formamidine acetate salt (1.88 mmol) was dissolved in 3 mL of isopropanol by adding 48% HBr (317 μL) in a separate vial.

Synthesis of Perovskite Nanocrystals by Hot Addition Method: $Cs_xFA_{(1-x)}PbBr_3$ PNCs were synthesized following the previously reported hot-addition method (HAM).[7] The $PbBr_2$ (1.88 mmol) in octadecene (40 mL) suspension was stirred and heated at 100 °C under vacuum for 1 h to remove traces of water. Afterward, OA (5 mL) and OLA (5 mL) were added to the suspension to dissolve $PbBr_2$. Formamidinium solution was injected into the Pb solution at 140 °C which turned the

solution to turbid green and then to light yellow as the temperature increased. For initial temperature rise to 170 °C nitrogen flow was introduced to remove 2-propanol and water. After 170 °C the nitrogen flow was stopped, and the temperature was increased in the nitrogen environment. The solution of cesium oleate (6 mL) was injected into the flask at 200 °C and the reaction was quenched by immersing the flask in an ice bath. The $Cs_xFA_{(1-x)}PbBr_3$ PNC in octadecene was directly used for the synthesis of the $CsPbBr_3/CsPb_2B_5$ composite.

Synthesis of $CsPbBr_3$ PNC: The $PbBr_2$ (1.88 mmol) in octadecene (40 mL) suspension was stirred and heated at 100 °C under vacuum for 1 h to remove traces of water. Afterward, OA (5 mL) and OLA (5 mL) were added to the suspension to dissolve $PbBr_2$ under a nitrogen environment. The solution of cesium oleate (6 mL) was injected into the flask at 200 °C and the reaction was quenched by immersing the flask in an ice bath. The $CsPbBr_3$ PNC in octadecene was directly used for post-synthesis treatment.

Fe^{3+} Assisted Synthesis of $CsPbBr_3/CsPb_2B_5$ 3D-in-2D Composites: $CsPbBr_3/CsPb_2B_5$ composites were synthesized by adding $Cs_xFA_{(1-x)}PbBr_3$ PNC in Fe^{3+} solution containing OA and OLA. To prepare the Fe^{3+} solution, $FeCl_3$, 0.5 mL of OA, and OLA were taken in a round bottom flask containing 10 mL of octadecene. The mixture was heated at 100 °C under a vacuum for 30 min to remove traces of water. After water removal, nitrogen flow was introduced, and $Cs_xFA_{(1-x)}PbBr_3$ PNC in octadecene was added. The solution was heated to 230 °C to form the $CsPbBr_3/CsPb_2B_5$ composites. To increase the size of 2D $CsPb_2Br_5$, the $FeCl_3$ percentage with respect to Pb was increased. The samples treated with 25, 50 and 100% of $FeCl_3$ were denoted as CF25, CF50, and CF100, respectively. The $Cs_xFA_{(1-x)}PbBr_3$ PNC solution was also heated with 0.5 mL of OA and OLA, but without $FeCl_3$, and the resulting composite was denoted as CF0. Synthesized samples were separated by centrifugation, and the precipitate was disbursed in toluene. Before obtaining the 3D-in-2D perovskite composite powder, the samples were washed with toluene twice by centrifugation.

Characterization: The absorption spectra were recorded using a UV–vis–NIR spectrophotometer (Cary 5000). Photoluminescence spectra were obtained with a Fluorolog-3 system (Horiba Jobin Yvon) using an excitation wavelength of 375 nm. The X-ray diffraction (XRD) pattern was obtained using a Panalytical X-Pert PRO MRD X-ray diffractometer equipped with a Cu X-ray source (Cu Kα, λ = 1.542 Å). The morphology of the prepared samples was analyzed by transmission electron microscopy (Thermo Scientific Talos F200X G2 200 kV). The energy dispersive x-ray (EDX) spectroscopy and mapping were carried out using the scanning transmission electron microscopy mode coupled with a bright field detector. For the TEM tilting experiment, a bright-field TEM image was acquired in TEM mode using a CCD camera with an acquisition time of 1 s. A Tomography Holder Fishione 2020 was used to tilt the sample. The PL transients were recorded with a time-correlated single-photon-counting (TCSPC) system (Fluotime 200, PicoQuant, excitation at 375 nm) from a picosecond pulsed-diode laser (LDH-375, PicoQuant, FWHM ≈70 ps). Top-view scanning electron microscopic images of thin film samples were measured by using SEM (JEOL JSM-7401F). Femtosecond transient absorption (TA) experiments were performed using an Excipro femtosecond transient absorption spectroscopic system (CDP system). The TA system utilizes an ultrashort pulse amplified laser pulse system (Coherent, Legend USP, 35 fs, 1 kHz, 795 nm, 3 mJ) as the light source for generating the pump and probe pulses. The pump pulse was generated by doubling the fundamental 795 nm laser pulse into 397 nm using a BBO crystal. A white light continuum generated by pumping a 5 mm sapphire crystal was used as a probe pulse. The probe light was limited to 750 nm using a short pass filter. The spot size of the pump pulse was ≈170 µm. The TA spectra were corrected for dispersion by measuring the optical Kerr signals of glass, and the background was corrected by subtracting the pump-only spectra. The laser fluence-dependent photoluminescence spectra were acquired using the TA spectroscopic system by blocking the probe pulse in the same transmission geometry used for TA experiments. The sample position was manually rasterized in between the measurements to avoid heating the samples due to intense pump pulses.

Supporting Information

Supporting Information is available from the Wiley Online Library or from the author.

Acknowledgements

This work was supported by the Natural Sciences and Engineering Research Council of Canada (NSERC RGPIN-2020-05921) and le Fonds de Recherche du Quebec–Nature et Technologies (FRQNT) through the Quebec Centre for Advanced Materials. D.M. is grateful to the Canada Research Chairs Program (CRC-2019-00253). The authors also gratefully acknowledge the support of the National Science and Technology Council (NSTC), Taiwan (Grant Nos. NSTC 111-2634-F-A49-007, NSTC 111-2123-M-A49-001, and NSTC 112-2639-M-A49-001-ASP) and the Center for Emergent Functional Matter Science of National Yang-Ming Chiao Tung University (NYCU) from the Featured Areas Research Center Program within the framework of the Higher Education Sprout Project by the Ministry of Education (MOE) in Taiwan.

Conflict of Interest

The authors declare no conflict of interest.

Data Availability Statement

The data that support the findings of this study are available from the corresponding author upon reasonable request.

Keywords

2D $CsPb_2Br_5$ nanosheet, 3D-in-2D nanocomposite, amplified stimulated emission, perovskite nanocrystals

Received: May 30, 2024
Revised: August 29, 2024
Published online:

[1] J. S. Manser, J. A. Christians, P. V. Kamat, *Chem. Rev.* **2016**, *116*, 12956.
[2] H. Aqoma, S.-H. Lee, I. F. Imran, J.-H. Hwang, S.-H. Lee, S.-Y. Jang, *Nat. Energy* **2024**, *9*, 324.
[3] Y. B. Cao, D. Zhang, Q. Zhang, X. Qiu, Y. Zhou, S. Poddar, Y. Fu, Y. Zhu, J.-F. Liao, L. Shu, B. Ren, Y. Ding, B. Han, Z. He, D.-B. Kuang, K. Wang, H. Zeng, Z. Fan, *Nat. Commun.* **2023**, *14*, 4611.
[4] B. Jeong, L. Veith, T. J. A. M. Smolders, M. J. Wolf, K. Asadi, *Adv. Mater.* **2021**, *33*, 2100486.
[5] K. Elkhouly, I. Goldberg, X. Zhang, N. Annavarapu, S. Hamdad, G. Croes, C. Rolin, J. Genoe, W. Qiu, R. Gehlhaar, P. Heremans, *Nat. Photonics* **2024**, *18*, 132.
[6] M.-C. Yen, C.-J. Lee, K.-H. Liu, Y. Peng, J. Leng, T.-H. Chang, C.-C. Chang, K. Tamada, Y.-J. Lee, *Nat. Commun.* **2021**, *12*, 4460.
[7] S. S. Bhosale, A. K. Kharade, S. Narra, S. Chang, E. Wei-Guang Diau, *ACS Energy Lett.* **2023**, *8*, 280.
[8] J. Shamsi, A. S. Urban, M. Imran, L. De Trizio, L. Manna, *Chem. Rev.* **2019**, *119*, 3296.
[9] L. C. Schmidt, A. Pertegás, S. González-Carrero, O. Malinkiewicz, S. Agouram, G. Mínguez Espallargas, H. J. Bolink, R. E. Galian, J. Pérez-Prieto, *J. Am. Chem. Soc.* **2014**, *136*, 850.
[10] L. Protesescu, S. Yakunin, M. I. Bodnarchuk, F. Krieg, R. Caputo, C. H. Hendon, R. X. Yang, A. Walsh, M. V. Kovalenko, *Nano Lett.* **2015**, *15*, 3692.

[11] F. Zhang, H. Zhong, C. Chen, X. Wu, X. Hu, H. Huang, J. Han, B. Zou, Y. Dong, *ACS Nano* **2015**, *9*, 4533.
[12] H. Huang, M. I. Bodnarchuk, S. V. Kershaw, M. V. Kovalenko, A. L. Rogach, *ACS Energy Lett.* **2017**, *2*, 2071.
[13] A. Swarnkar, W. J. Mir, A. Nag, *ACS Energy Lett.* **2018**, *3*, 286.
[14] S. S. Bhosale, S. Narra, E. Jokar, A. Manikandan, Y.-L. Chueh, E. W.-G. Diau, *J. Mater. Chem. C* **2021**, *9*, 17341.
[15] A. Dey, J. Ye, A. De, E. Debroye, S. K. Ha, E. Bladt, A. S. Kshirsagar, Z. Wang, J. Yin, Y. Wang, L. N. Quan, F. Yan, M. Gao, X. Li, J. Shamsi, T. Debnath, M. Cao, M. A. Scheel, S. Kumar, J. A. Steele, M. Gerhard, L. Chouhan, K. Xu, X. G. Wu, Y. Li, Y. Zhang, A. Dutta, C. Han, I. Vincon, A. L. Rogach, et al., *ACS Nano* **2021**, *15*, 10775.
[16] S. K. Avugadda, A. Castelli, B. Dhanabalan, T. Fernandez, N. Silvestri, C. Collantes, D. Baranov, M. Imran, L. Manna, T. Pellegrino, M. P. Arciniegas, *ACS Nano* **2022**, *16*, 13657.
[17] D. Guggisberg, S. Yakunin, C. Neff, M. Aebli, D. Günther, M. V. Kovalenko, D. N. Dirin, *Chem. Mater.* **2023**, *35*, 2827.
[18] V. K. Ravi, S. Saikia, S. Yadav, V. V. Nawale, A. Nag, *ACS Energy Lett.* **2020**, *5*, 1794.
[19] I. Rosa-Pardo, A. Ciccone, R. Arenal, R. E. Galian, J. Pérez-Prieto, *Chem. Mater.* **2023**, *35*, 7011.
[20] L. Ding, B. Borjigin, Y. Li, X. Yang, X. Wang, H. Li, *ACS Appl. Mater. Interfaces* **2021**, *13*, 51161.
[21] V. Drushliak, M. Szafrański, *Inorg. Chem.* **2022**, *61*, 14389.
[22] S. K. Balakrishnan, P. V. Kamat, *Chem. Mater.* **2018**, *30*, 74.
[23] P. Gao, Z. Cui, X. Liu, Y. Wu, Q. Zhang, Z. Wang, Z. Zheng, H. Cheng, Y. Liu, Q. Li, B. Huang, P. Wang, *Chem. - Eur. J.* **2022**, *28*, 202201095.
[24] L. Ruan, W. Shen, A. Wang, A. Xiang, Z. Deng, *J. Phys. Chem. Lett.* **2017**, *8*, 3853.
[25] Y. Zhou, Y. Yu, Y. Zhang, X. Liu, H. Yang, X. Liang, W. Xia, W. Xiang, *Inorg. Chem.* **2021**, *60*, 3814.
[26] G. Jiang, C. Guhrenz, A. Kirch, L. Sonntag, C. Bauer, X. Fan, J. Wang, S. Reineke, N. Gaponik, A. Eychmüller, *ACS Nano* **2019**, *13*, 10386.
[27] Y. Zhang, T. D. Siegler, C. J. Thomas, M. K. Abney, T. Shah, A. De Gorostiza, R. M. Greene, B. A. Korgel, *Chem. Mater.* **2020**, *32*, 5410.
[28] A. J. Harding, K. D. Dobson, B. A. Ogunnaike, W. N. Shafarman, *Phys. Status Solidi* **2021**, *218*, 2100246.
[29] C. C. Stoumpos, C. D. Malliakas, J. A. Peters, Z. Liu, M. Sebastian, J. Im, T. C. Chasapis, A. C. Wibowo, D. Y. Chung, A. J. Freeman, B. W. Wessels, M. G. Kanatzidis, *Cryst. Growth Des.* **2013**, *13*, 2722.
[30] Z. Zhang, Y. Zhu, W. Wang, W. Zheng, R. Lin, F. Huang, *J. Mater. Chem. C* **2018**, *6*, 446.
[31] Z. Liu, Y. Bekenstein, X. Ye, S. C. Nguyen, J. Swabeck, D. Zhang, S. T. Lee, P. Yang, W. Ma, A. P. Alivisatos, *J. Am. Chem. Soc.* **2017**, *139*, 5309.
[32] T. Li, N. Dang, W. Zhang, W. Liang, F. Yang, *Nanomaterials* **2018**, *8*, 991.
[33] G. Nedelcu, L. Protesescu, S. Yakunin, M. I. Bodnarchuk, M. J. Grotevent, M. V. Kovalenko, *Nano Lett.* **2015**, *15*, 5635.
[34] Q. A. Akkerman, V. D'Innocenzo, S. Accornero, A. Scarpellini, A. Petrozza, M. Prato, L. Manna, *J. Am. Chem. Soc.* **2015**, *137*, 10276.
[35] M. Grabolle, M. Spieles, V. Lesnyak, N. Gaponik, A. Eychmüller, U. Resch-Genger, *Anal. Chem.* **2009**, *81*, 6285.
[36] Y. Yuan, G. Yan, C. Dreessen, T. Rudolph, M. Hülsbeck, B. Klingebiel, J. Ye, U. Rau, T. Kirchartz, *Nat. Mater.* **2024**, *23*, 391.
[37] S. Zou, X. Zhao, J. Lyu, W. Ouyang, R. Liu, S. Xu, *J. Phys. Chem. Lett.* **2023**, *14*, 4815.
[38] L. Huang, Q. Gao, L. Sun, H. Dong, S. Shi, T. Cai, Q. Liao, C. Yan, *Adv. Mater.* **2018**, *30*, 1800596.
[39] L. Jiang, R. Liu, R. Su, Y. Yu, H. Xu, Y. Wei, Z. K. Zhou, X. Wang, *Nanoscale* **2018**, *10*, 13565.
[40] Y. Li, H. Hu, A. Farag, T. Feeney, I. Allegro, U. Lemmer, U. W. Paetzold, I. A. Howard, *Nano Lett.* **2023**, *23*, 1637.
[41] M. Athanasiou, A. Manoli, P. Papagiorgis, K. Georgiou, Y. Berezovska, A. Othonos, M. I. Bodnarchuk, M. V. Kovalenko, G. Itskos, *ACS Photonics* **2022**, *9*, 2385.
[42] M. Li, Q. Shang, C. Li, S. Li, Y. Liang, W. Yu, C. Wu, L. Zhao, Y. Zhong, W. Du, X. Wu, Z. Jia, Y. Gao, H. Chen, X. Liu, S. Guo, Q. Liao, G. Xing, L. Xiao, Q. Zhang, *Adv. Funct. Mater.* **2021**, *31*, 2102210.
[43] H. Zhu, Y. Fu, F. Meng, X. Wu, Z. Gong, Q. Ding, M. V. Gustafsson, M. T. Trinh, S. Jin, X.-Y. Zhu, *Nat. Mater.* **2015**, *14*, 636.
[44] S. Cheng, Q. Chang, Z. Wang, L. Xiao, E. E. M. Chia, H. Sun, *Adv. Opt. Mater.* **2021**, *9*, 2100564.
[45] D. Kim, H. Ryu, S. Y. Lim, K. M. McCall, J. Park, S. Kim, T. J. Kim, J. Kim, Y. S. Kim, M. G. Kanatzidis, H. Cheong, J. I. Jang, *Chem. Mater.* **2021**, *33*, 7185.
[46] D. Vila-Liarte, M. W. Feil, A. Manzi, J. L. Garcia-Pomar, H. Huang, M. Döblinger, L. M. Liz-Marzán, J. Feldmann, L. Polavarapu, A. Mihi, *Angew. Chem., Int. Ed.* **2020**, *59*, 17750.
[47] P. Geiregat, J. Maes, K. Chen, E. Drijvers, J. De Roo, J. M. Hodgkiss, Z. Hens, *ACS Nano* **2018**, *12*, 10178.
[48] E. Kobiyama, H. Tahara, R. Sato, M. Saruyama, T. Teranishi, Y. Kanemitsu, *Nano Lett.* **2020**, *20*, 3905.
[49] G. Yumoto, H. Tahara, T. Kawawaki, M. Saruyama, R. Sato, T. Teranishi, Y. Kanemitsu, *J. Phys. Chem. Lett.* **2018**, *9*, 2222.
[50] Y. Liu, Y. Li, K. Gao, J. Zhu, K. Wu, *J. Am. Chem. Soc.* **2023**, *145*, 25864.
[51] V. I. Klimov, A. A. Mikhailovsky, S. Xu, A. Malko, J. A. Hollingsworth, C. A. Leatherdale, H.-J. Eisler, M. G. Bawendi, *Science* **2000**, *290*, 314.
[52] Y. Xu, Q. Chen, C. Zhang, R. Wang, H. Wu, X. Zhang, G. Xing, W. W. Yu, X. Wang, Y. Zhang, M. Xiao, *J. Am. Chem. Soc.* **2016**, *138*, 3761.